AFRL-RY-WP-TR-2018-0025

LOW POWER OPTICAL PHASE ARRAY USING GRAPHENE ON SILICON PHOTONICS

Ipshita Datta, Brian Lee, and Michal Lipson

Columbia University in the City of New York

MARCH 2018
Final Report

AIR FORCE RESEARCH LABORATORY
SENSORS DIRECTORATE
WRIGHT-PATTERSON AIR FORCE BASE, OH 45433-7320
AIR FORCE MATERIEL COMMAND
UNITED STATES AIR FORCE

NOTICE AND SIGNATURE PAGE

Using Government drawings, specifications, or other data included in this document for any purpose other than Government procurement does not in any way obligate the U.S. Government. The fact that the Government formulated or supplied the drawings, specifications, or other data does not license the holder or any other person or corporation; or convey any rights or permission to manufacture, use, or sell any patented invention that may relate to them.

This report is the result of contracted fundamental research deemed exempt from public affairs security and policy review in accordance with SAF/AQR memorandum dated 10 Dec 08 and AFRL/CA policy clarification memorandum dated 16 Jan 09. This report is available to the general public, including foreign nationals.

Copies may be obtained from the Defense Technical Information Center (DTIC) (http://www.dtic.mil).
AFRL-RY-WP-TR-2017-0096 HAS BEEN REVIEWED AND IS APPROVED FOR PUBLICATION IN ACCORDANCE WITH ASSIGNED DISTRIBUTION STATEMENT.

// Signature//

ATTILA A. SZEP
Program Manager and Branch Chief
Integrated Circuits & Microsystems Branch
Aerospace Components & Subsystems Division

// Signature//

JAMES M. SATTLER, Lt Col, USAF
Deputy
Aerospace Components & Subsystems Division
Sensors Directorate

This report is published in the interest of scientific and technical information exchange, and its publication does not constitute the Government's approval or disapproval of its ideas or findings.

*Disseminated copies will show "//Signature//" stamped or typed above the signature blocks.

REPORT DOCUMENTATION PAGE

Form Approved
OMB No. 0704-0188

1. REPORT DATE *(DD-MM-YY)*	2. REPORT TYPE	3. DATES COVERED *(From - To)*
March 2018	Final	2 June 2016 – 2 December 2017

4. TITLE AND SUBTITLE
LOW POWER OPTICAL PHASE ARRAY USING GRAPHENE ON SILICON PHOTONICS

5a. CONTRACT NUMBER
FA8650-16-1-7643

5b. GRANT NUMBER

5c. PROGRAM ELEMENT NUMBER
62716E

6. AUTHOR(S)
Ipshita Datta, Brian Lee, and Michal Lipson

5d. PROJECT NUMBER
N/A

5e. TASK NUMBER
N/A

5f. WORK UNIT NUMBER
Y1G6

7. PERFORMING ORGANIZATION NAME(S) AND ADDRESS(ES)
Columbia University in the City of New York
116th St & Broadway
New York, NY 10027

8. PERFORMING ORGANIZATION REPORT NUMBER

9. SPONSORING/MONITORING AGENCY NAME(S) AND ADDRESS(ES)
Air Force Research Laboratory
Sensors Directorate
Wright-Patterson Air Force Base, OH 45433-7320
Air Force Materiel Command
United States Air Force

Defense Advanced Research Projects Agency
DARPA/MTO
675 North Randolph Street
Arlington, VA 22203

10. SPONSORING/MONITORING ACRONYMS
AFRL/RYDI

11. SPONSORING/MONITORING AGENCY REPORT NUMBER(S)
AFRL-RY-WP-TR-2018-0025

12. DISTRIBUTION/AVAILABILITY STATEMENT
Approved for public release; distribution is unlimited.

13. SUPPLEMENTARY NOTES
This report is the result of contracted fundamental research deemed exempt from public affairs security and policy review in accordance with SAF/AQR memorandum dated 10 Dec 08 and AFRL/CA policy clarification memorandum dated 16 Jan 09. This material is based on research sponsored by Air Force Research Laboratory (AFRL) and the Defense Advanced Research Agency (DARPA) under agreement number FA8650-14-1-7415. The U.S. Government is authorized to reproduce and distribute reprints for Governmental purposes notwithstanding any copyright notation herein. The views and conclusions contained herein are those of the authors and should not be interpreted as necessarily representing the official policies of endorsements, either expressed or implied, of AFRL and DARPA or the U.S. Government. Report contains color.

14. ABSTRACT
In this report, Columbia University investigated the potential of using low loss and low power graphene phase shifter for integrated silicon photonics. The work developed the critical steps for a platform consisting of 2D materials embedded in waveguides, in which electrostatic doping is used for tuning the dielectric properties of the guiding structures. Graphene as well as other 2D materials and thin films, have been shown recently to exhibit high tunability of index with doping. This platform could enable ultrafast devices with unprecedented low power.

15. SUBJECT TERMS
graphene phase modulator, silicon photonics, optical phase array

16. SECURITY CLASSIFICATION OF:			17. LIMITATION OF ABSTRACT:	18. NUMBER OF PAGES	19a. NAME OF RESPONSIBLE PERSON (Monitor)
a. REPORT	b. ABSTRACT	c. THIS PAGE			Attila Szep
Unclassified	Unclassified	Unclassified	SAR	34	19b. TELEPHONE NUMBER *(Include Area Code)* N/A

Table of Contents

Section **Page**

List of Figures ii
PREFACE 1
1. SUMMARY 2
2. INTRODUCTION 3
2.1 Background 3
2.1.1 Graphene's Electro-Optic Properties 3
2.1.2 Graphene Bandwidth and Contacts 4
2.2 Approach 5
2.2.1 Modulators 5
2.2.2 Graphene Edge Contacts 6
3. METHODS, ASSUMPTIONS, AND PROCEDURES 7
3.1 Theory and Methodology 7
3.2 Transmission Line Method to Measure Graphene Contact Resistance 9
3.3 Fabrication 10
4. RESULTS AND DISCUSSION 15
4.1 Graphene Electro-Refractive Modulator 15
4.1.1 Change in MZI Transmission after using Ammonium Persulfate 17
4.1.2 MID IR Modulation by Graphene 22
4.2 Graphene Edge Contacts 23
5. CONCLUSIONS 26
6. RECOMMENDATIONS 27
7. REFERENCES 28
LIST OF ABBREVIATIONS, ACRONYMS, AND SYMBOLS 29

List of Figures

Figure **Page**

Figure 1: Graphene's Electro-Optic Properties 4
Figure 2: Circuit Model of a Graphene Modulators Utilizing Graphene-Dielectric-Graphene Structure 5
Figure 3: Graphene Edge Contacts 6
Figure 4: Theoretical Complex Optical Conductivity of Graphene for different Intra-Band Scattering Rates 8
Figure 5: Principle of Operation of Graphene-HfO_2-Graphene Capacitor 9
Figure 6: TLM to Measure Graphene Contact Resistance 10
Figure 7: Fabrication Flow for the Graphene Devices 11
Figure 8: Fabrication Flow for Graphene Edge Contacts 12
Figure 9: The Effect of Side Wall Angle in Forming Graphene Edge Contacts 13
Figure 10: SEM Image of the Redespoited Sidewalls and how BOE Dip can Remove this Residue 14
Figure 11: Electrical and Optical Measurements - Effective Index and Absorption Profile of the Propagating TE Mode with different Voltages Applied to the Graphene Capacitor on the Right Arm 15
Figure 12: Electrical and Optical Measurements - Refractive Index and Absorption of Top and Bottom Graphene Sheets Obtained from Figure 2 and COMSOL Simulations 16
Figure 13: RC Frequency Response of the Capacitive Devices 16
Figure 14: Graphene Devices Fabricated using New Ammonium Persulphate Transfer Method 17
Figure 15: MZI Transmission with Voltage 18
Figure 16: Extracted Graphene Absorption Modulation at different Bias Voltages at 1550 nm 18
Figure 17: MZI Transmission for Devices when Graphene is initially p-doped 19
Figure 18: MZI Transmission when Graphene is Unbiased initially 19
Figure 19: COMSOL Simulated Effective Index Change for Waveguide Configuration 2 um Wide x 530 nm Tall Waveguides 20
Figure 20: Theoretical Transmission in a balanced Mach Zehnder at different Voltages Applied across the Top and Bottom Electrode 21
Figure 21: Measured Transmission vs Wavelength at different Bias Voltages when the Substrate is Heated to 30 C 21
Figure 22: Extracted Aborption in Graphene vs Voltage and Comparison with Theory 22
Figure 23: MZI Transmission Output Extinction Ratio vs Voltage for Mid IR Wavelengths 22
Figure 24: First Generation of Graphene Edge Contacts 24
Figure 25: Resistance Normalized to Width with Respect to graphene Channel Length 24
Figure 26: CVD Graphene Transfer Tears and Residues 25

PREFACE

This report looks into the potential of using Graphene Phase Modulators to design low power, low loss and low drive voltages. The state of the art phase shifters have a high power comsumption of 8.5 mW per π phase shift. The phase shift is typically induced through thermal tuning, which results in high power dissipation. A 1000 x 1000 array of such element will comsume on an average of 4.35 kW. Thermal tuning also limits the speed of the devices to 100 kHz. The proposed graphene phase modulator is aimed to have low power comsumption of 1.3 uW per π phase shift and no direct current (DC) power consumption. Phase shift is induced through the linear electro-optic (EO) effect. A 1000 x 1000 array will have a power consumption of 650 mW. The potential of using a capacitive thin film integrated capacitor can render any passive platform active through the modal interaction, thereby enabling novel applications. In addition, this report looks into methods to improve graphene-metal contact resistance – a long standing problem in two-dimensional (2D) materials. Low contact-resistance is crucial for achieving high bandwidth, as high resistance negatively contributes to the resistor-capacitor (RC) bandwidth of the modulator. The state of the art graphene contacts achieve low contact resistance either by using clean and high quality exfoliated graphene sheets or exotic cleaning techniques, such as laser cleaning, which limits the scalability for wafer scale applications with high device density.

1. SUMMARY

We show in this report that graphene can provide electro-optic properties to traditionally passive optical materials. We show a 0.6 GHz electro-refractive modulator with $V_{\pi}L$ of 1.4 Vcm based on graphene layers integrated with a silicon nitride waveguide. Under applied voltage, we experimentally reach the theoretically predicted anomalous regime of the graphene index, where the real part of the index is changed by 250 percent while its imaginary part (i.e. the absorption) remains largely unchanged. Moreover, we developed a process for reducing contact resistance of embedded graphene in photonic strutures, using using scalable chemical vapor deposition (CVD) grown graphene, which enables large scale fabrication high density graphene-based electro-optic devices. We measured our CVD graphene contact resistance of 1.2 kΩ-μm at the Dirac point of graphene (minimal carrier density), where the contact-resistance value is the highest. This value is apporximatelly one order of magnitude higher than measured without the optimized process, and it is sufficient to ensure that 30 GHz operation. We believe the contact resistance value can be at least an order of magnitude lower with higher carrier gating of graphene, such as a typical bias point for graphene phase modulators. This opens the door to higher bandwidth phase modulators.

2. INTRODUCTION

2.1 Background

2.1.1 Graphene's Electro-Optic Properties

Despite enormous advances in integrated photonics over the last decade, an efficient integrated phase delay remains to be demonstrated. This problem is fundamental- most monolithic thin film deposition relies on centro symmetric materials (such as silicon, silicon dioxide, silicon nitride), which by definition do not have an electro-optic effect. Such materials have been shown to be excellent transparent materials, however they are either optically passive, or rely on very small plasma dispersion effect or power-hungry thermo-optic effect for tunability. These phase change materials have losses associated due to heating or carrier injection in the waveguides. Here we show that graphene can be used to provide electro-optic properties to traditionally passive optical materials.

Graphene is a versatile 2D material with wavelength-insensitive electrical tunability of its optical absorption and refractive index (Figure 1). As seen in Figure 1, theory predicts a strong tenability of the graphene's optical properties with tuning of the Fermi level. This tuning is achieved here via electrostatic doping by embedding the graphene in a capacitor (as shown in Figure 1c). As the Fermi level is tuned, it is predicted that the absorption decreases (region I). As the tuning is further increased, the absorption becomes negligible, while the index of refraction changes drastically (region II and III). The ease of integration with silicon photonics and the capacitive nature of graphene electro-optic devices renders graphene an attractive choice for photonics. The electrostatic tunability of the optical properites of graphene lends graphene the novel capability of transcending any passive platform to an active device.

To date, the state of the art graphene electro-optic modulators level has been mostly designed using the voltage tunable absorption of graphene [1,2]. The potential of utilizing the voltage dependent refractive index tunability of graphene has been recently demonstrated in [5,6,7]. In these devices, however, the phase modulation is accompanied by loss modulation at low voltages of operation, where absorption and refractive index gets tuned simultaneously. In [8,9], the regime of low loss and high refractive index of graphene has been electrostatically tuned using electrolytic ion gels, which render these devices low speed. Using the current Silicon-insulator-graphene configuration in [8,9], the authors have not yet achieved the regime where the absorption of graphene is low and the phase change is high. Their device is limited within the fermi energy level of 0.5 eV (region I of Figure 1a), where loss and phase change proceed simultaneously. Recently, the devices demonstrated have limited speed of operation since they use electrolyte, whereas the silicon–insulator-graphene configuration are limited to the high loss and phase change regime (region I of Figure 1a).

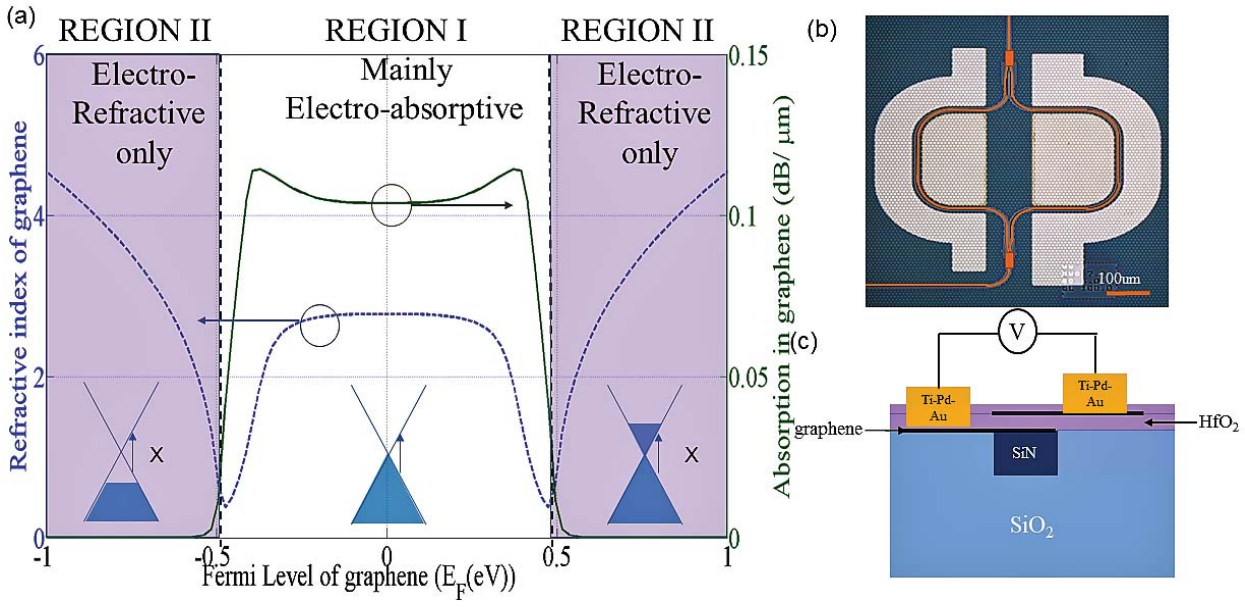

Figure 1: Graphene's Electro-Optic Properties

(a) Theoretical absorption and refractive index as a function of Fermi level for intrinsic graphene (region I – high absorption, region II – low absorption). (b) Optical micrograph of the fabricated device (interferometer arms false colored). (c) Device cross section showing graphene-HfO_2-graphene capacitor on Si_3N_4 waveguide.

2.1.2 Graphene Bandwidth and Contacts

Achieving low contact resistance between graphene and metal electrodes is crucial for high speed graphene-based electro-optic devices. Standard surface contacts (such as the ones shown schematically in Figure 2) , in general have extremely high resostance since graphene lacks vertical surface bonding sites.

The graphene modulator's operation bandwidth is not practically limited by the carrier transport in graphene, but it is bottlenecked by the parasitic components of the modulator circuit. These parasitics are the capacitor formed by the graphene-dielectric-graphene stack, graphene-sheet resistance, and graphene-metal contact resistance. Figure 2 describes an equivalent circuit model of a graphene modulators utilizing graphene-dielectric-graphene structure. In bottom inset of Figure 2, R_{source} is the source impedance, $R_{contact}$ is the contact resistance from the graphene-metal interface, R_{sheet} is the resistance from the graphene sheet, and C is the capacitance of the modulator. The electro-optic bandwidth is approximately modeled by the RC bandwidth, where the cutoff frequency, f_c, is approximately equal to $1/(2\pi R_{total}C)$, where $R_{total} = R_{source} + 2(R_{contact} + R_{sheet})$. While it is possible to engineer the device footprint to reduce the capacitance and the sheet resistance, for example, by reducing the width and length of the graphene and dielectric spacing between the graphene layers, the contact resistance is fundamentally related to how the metal-graphene interface is formed. Typically, surface contacts have been employed to interface the metal and the graphene surface, where the metal is deposited at the graphene's top surface in order to form contacts. The metal and graphene interaction in the surface contacts approach occurs perpendicularly to the graphene molecular 2D plane. Since graphene lacks vertical

surface bonding sites, surface contacts are fundamentally incapable of maximizing metal and graphene interaction due to weak orbital hybridization and chemical bonding with the metal. [10]

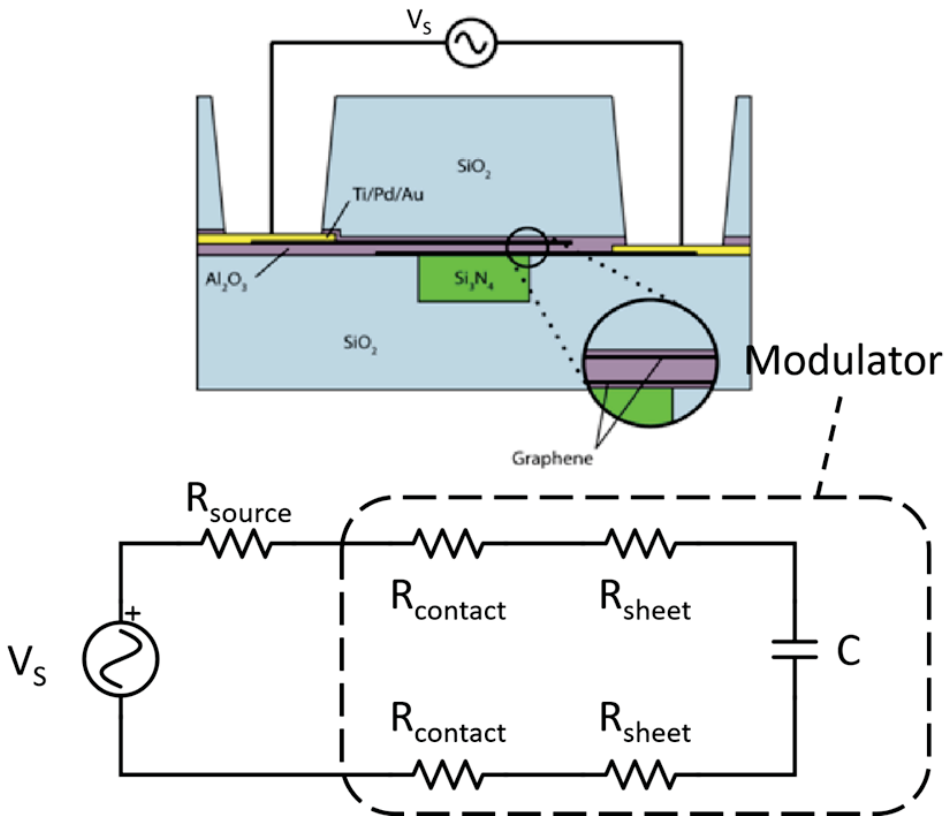

Figure 2: Circuit Model of a Graphene Modulators Utilizing Graphene-Dielectric-Graphene Structure

(Top) Schematic of a graphene modulator from Ref. [7]. It has graphene-dielectric-graphene stack on top of a Si_3N_4 waveguide to modulate the optical mode. (Bottom) Equivalent circuit of the modulator. Rsource is the source impedance, Rcontact is the contact resistance from the graphene-metal interface, Rsheet is the resistance from the graphene sheet, and C is the capacitance of the modulator.

2.2 Approach

2.2.1 Modulators

In this report, we show a modulator that achieves in the theoretically predicted regime where only the phase is modulated while the absorption of the graphene remains low. Figure 1a shows the different regimes of the absorption and refractive index (optical permittivity) of graphene dependent on the Fermi level [3,4,5] which can be electrically tuned. In order to reach the regime where only the real part of refractive index is modulated, one needs to apply high electric field across the graphene-insulator-graphene capacitor (region II in Figure 1a), a challenging task due to the dielectric breakdown of the oxides commonly used in silicon photonics [1,2] , Mohsin et al. [6] have recently demonstrated EO modulation using the voltage-dependent refractive index,

but their device is accompanied by loss modulation due to the low operating voltages (region I in Figure 1a).

In order to achieve the regime where only the phase is modulated, we design a modulator with embedded high-K and high breakdown dielectric (Hafnia, HfO_2) for enabling large modulation of the Fermi level (Figure 1b,c). This allows the graphene to be biased into the low-loss regime with no inter-band transitions. To test phase modulation, we fabricate an unbalanced integrated Mach-Zender interferometer (MZI) with 100 μm length of the graphene-HfO_2-graphene capacitor on both arms. The interferometer arms are designed with 1 μm wide x 300 nm tall Si_3N_4 waveguides for single mode (transverse electric (TE)) propagation at 1560 nm. The fabrication follows the process described in [2], except that HfO_2 is used as a dielectric between the two CVD graphene layers.

2.2.2 Graphene Edge Contacts

In order to overcome the typically high resistance of graphene devices, we fabricated graphene contacts that interface between the metal and graphene sheets via graphene in-plane edges [10] (see Figure 3) by utilizing highly scalable CVD graphene and atomic layer deposition (ALD) HfO_2 dielectric layers. Interfacing metal and graphene along the graphene edge has the potential to fundamentally reduce the contact resistance by interfacing the metal with graphene in the strong in-plane hybridization direction of the graphene. We also encapsulate the graphene layer with ALD HfO_2 on the top and bottom to serve as graphene protection as well as to ensure that only the graphene in-plane edges are exposed to the metal. Figure 3 describes this approach.

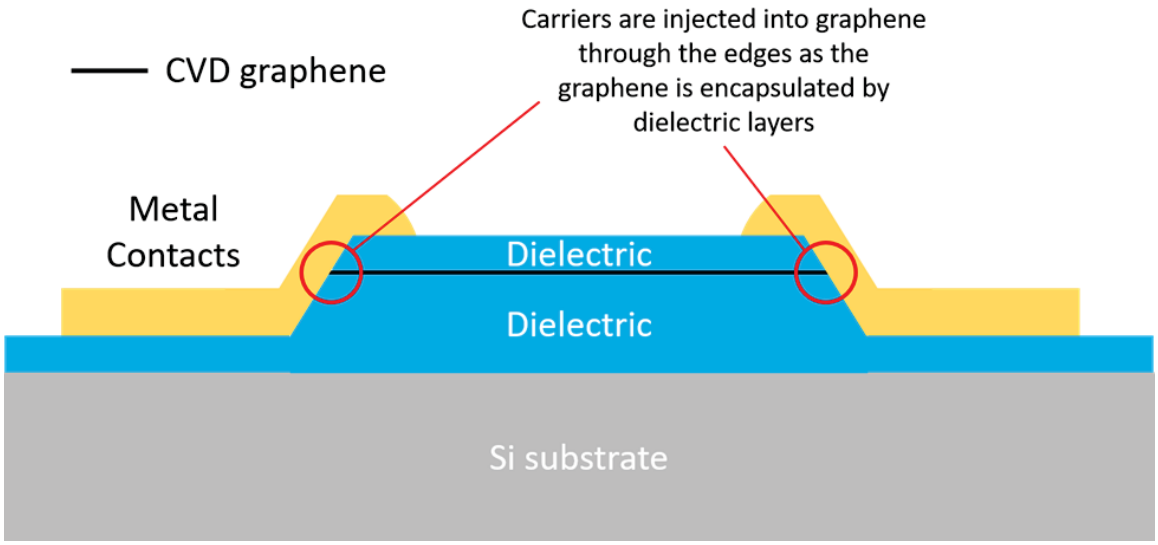

Figure 3: Graphene Edge Contacts
Graphene layer is encapsulated by dielectric layer on top and bottom. By etching this stack, it allows to expose the graphene edge, where subsequent deposition of metal will only allow metal-graphene contact at the edges of the graphene.

3. METHODS, ASSUMPTIONS, AND PROCEDURES

3.1 Theory and Methodology

The optical properties of 2D graphene can be modified electrically and, according to theory [1,2], the real part of the refractive index (RI) can be tuned without altering the imaginary part (i.e. absorption). The optical properties of graphene can be tuned by doping graphene electrostatically, i.e. by applying a voltage *V* across a graphene-insulator-graphene capacitor. The doping of graphene induces a shift in the Fermi energy level of graphene, given by:

$$E_F = \hbar v_F \left(\left(\frac{\epsilon_0 \epsilon_R V}{de} + n_{initial} \right) \pi \right)^{1/2} \quad (1)$$

where, ϵ_0 is the vacuum permittivity, ϵ_R is the relative permittivity of the insulator, e is the electronic charge, v_F is the Fermi velocity in graphene and $n_{initial}$ is the initial chemical doping of the graphene layer (which is dependent on the processing of the graphene and on the substrate [3,4]). The real part (n_R) and imaginary part (n_I) of the RI of graphene are related to the optical conductivity $\sigma(\omega)$ through equations 2 and 3.

$$(n_R + i n_I)^2 = 1 + \frac{i\sigma(\omega)}{\hbar \omega t} \quad (2)$$

$$\sigma(\omega) = \frac{\sigma_0}{2}\left(tanh\frac{\hbar\omega + 2E_F}{4k_B T} + tanh\frac{\hbar\omega - 2E_F}{4k_B T} \right) - i\frac{\sigma_0}{2\pi} log\left[\frac{(\hbar\omega + 2E_F)^2}{(\hbar\omega - 2E_F)^2 + (2k_B T)^2} \right] + i\frac{4\sigma_0}{\pi}\frac{E_F}{\hbar\omega + i\frac{\hbar}{\tau}} \quad (3)$$

where t is the thickness of the graphene layer (= 0.345 nm), σ_0 is the universal conductivity of graphene, ħ is the reduced Planck's constant, ω is the optical frequency, k_B is the Boltzmann constant, T is the temperature and τ is the intra-band carrier relaxation time, assumed here to be 100 fs, as predicted for similar structures [5]. This dependence is shown in Figure 1a (solid lines) where in the predicted anomalous region, the n_R changes by an order of magnitude, while the n_I (absorption) remains low.

The real and imaginary part of the complex optical conductivity is shown in Figure 4 with different intra-band scattering rates. It is difficult to reach the anomalous regime in an integrated, high-speed device because the required high electric fields (2.5 – 3.5 MV/cm) approach typical breakdown fields of thin-film oxides. To date this regime of high index change and low absorption has only been achieved by using ion/electrolyte gel gating [6], which is a fundamentally slow process. The low breakdown strength of the dielectrics have limited the state-of-the-art integrated graphene devices to modulating only the n_I of graphene [7,8].

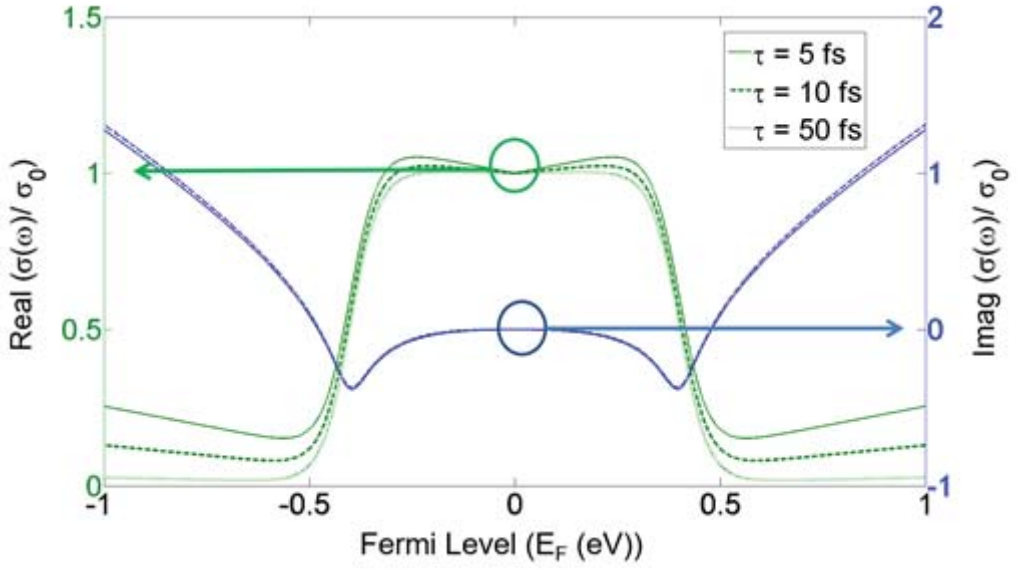

Figure 4: Theoretical Complex Optical Conductivity of Graphene for different Intra-Band Scattering Rates

In order to achieve the predicted regime we use the configuration described in Figure 5. 2D monolayer graphene behaves as a bipolar material, which suggests that the graphene sheet can either be p-doped or n-doped by extracting or injecting electrons in the sheets. Graphene is also a good conductor with mobilities in CVD graphene reaching about 1000 $cm^2/(V.s)$. These two features render graphene as an excellent material for creating the two conductors in a parallel plate capacitor configuration. The parallel plate capacitor configuration can be used to introduce electrons in one sheet and extract electrons from the other sheet. The measure of the electric fields or voltage/distance that can be applied across the two electrodes in a parallel plate capacitor is determined by the dielectric constant and the breakdown fields which the dielectric separating the two electrodes can tolerate. We use a high-K and high breakdown dielectric.

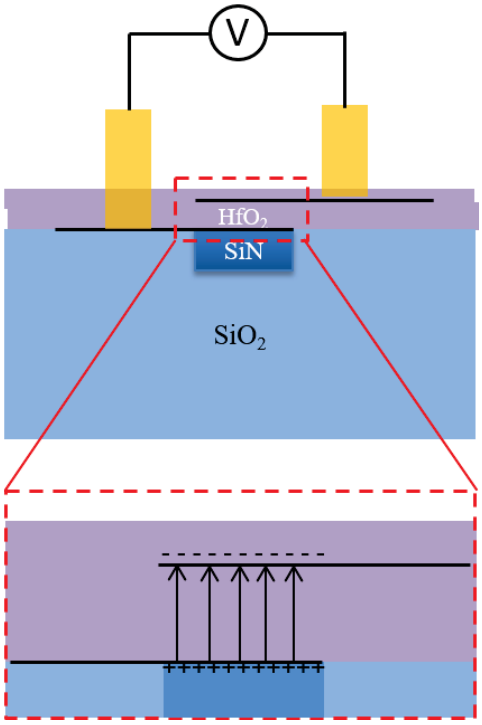

Figure 5: Principle of Operation of Graphene-HfO_2-Graphene Capacitor

3.2 Transmission Line Method to Measure Graphene Contact Resistance

Transmission line method (TLM) is used to measure the contact resistance in graphene devices. Figure 6 describes how TLM can be used to measure the contact resistance. We fabrictate TLM test structures that consists of graphene channels with various lengths. We measure the resistance of the channels and plot the resistance vs length, as shown in Figure 6b. If we normalize the resistance values by the width of the graphene channel, and find the y-intercept of the linear fit, this intercept is the resitance contribution from the two contacts of the graphene channel. We can extrapolate the contact resistance from this y-intercept of the linear fit, i.e., the contact resistance, R_c, is equal to the half of this y-intercept.

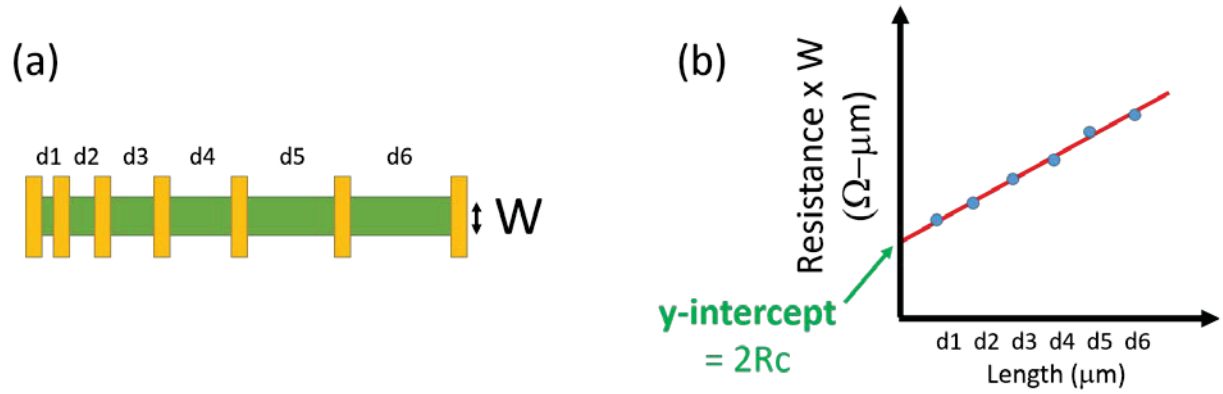

Figure 6: TLM to Measure Graphene Contact Resistance

(a) A schematic of a TLM test structure. Green strip is the graphene channel with width W. Yellow rectangles are metal contacts, and are separated with various separation distances d_i ($i = 1, 2, \ldots$). (b) This example of a TLM plot describes how to extract the contact resistance. By measuring and linearly fitting the resistance normalized by the channel width ($R \times W$) at various channel lengths, y-intercept of the fit ($d = 0$) is the resistance contribution of two contacts. Therefore, the contact resistance, R_c, is equal to half of the y-intercept of this fit.

3.3 Fabrication

The fabrication of the integrated graphene MZI's and devices is detailed in Figure 7.

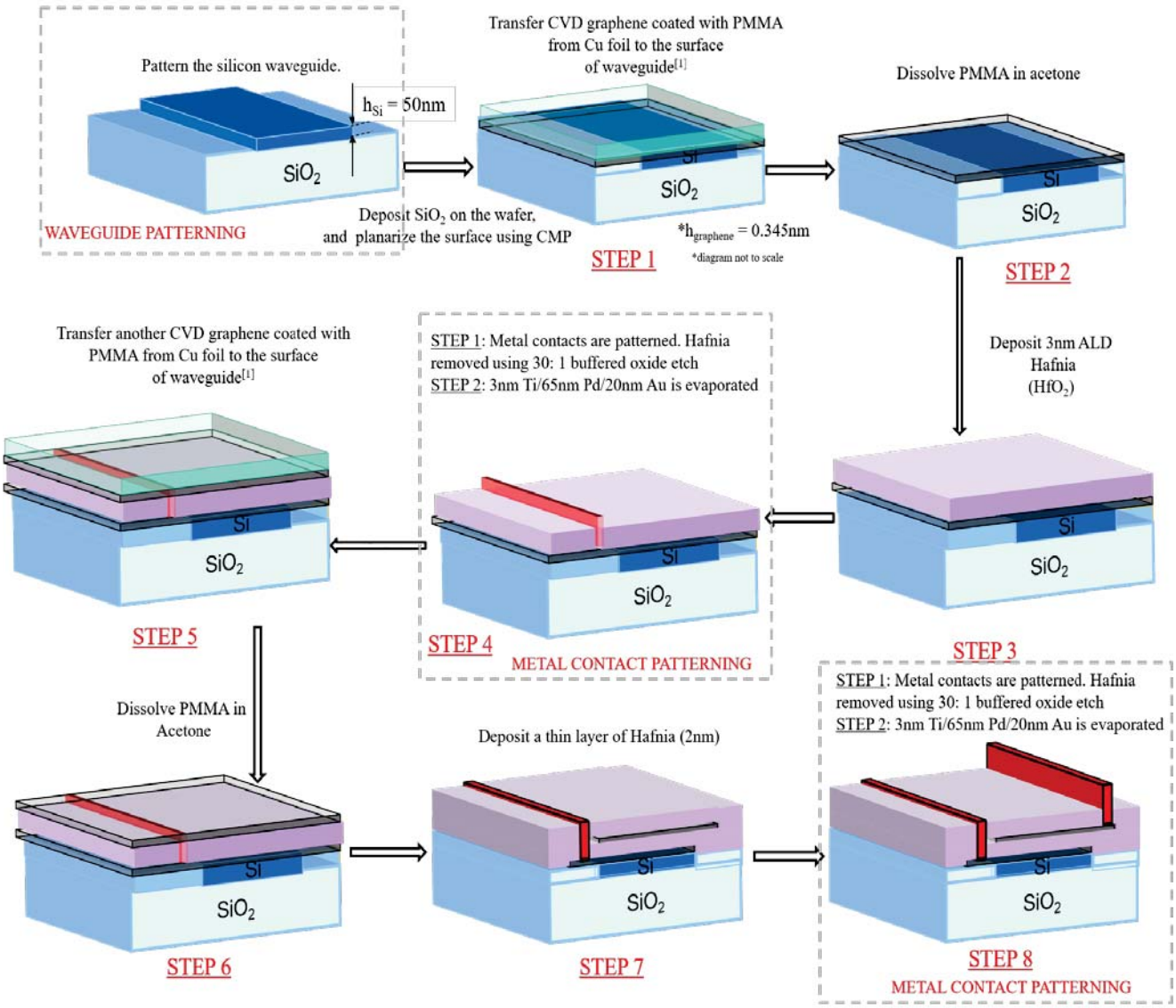

Figure 7: Fabrication Flow for the Graphene Devices

The fabrication of graphene edge contacts is detailed in Figure 8. The critical steps in fabricating graphene edge contacts is STEP 5 and STEP 6 in Figure 8. In STEP 5, it is critical to etch the graphene stack with an angled-etch as opposed to vertical side wall etch. During metal evaporation, the metal may not form contact with graphene because evaporation is vertical and anisotropic. The angled side wall of the stack ensures that the graphene edge is exposed and that the metal can form contact. Figure 9 illustrates this point.

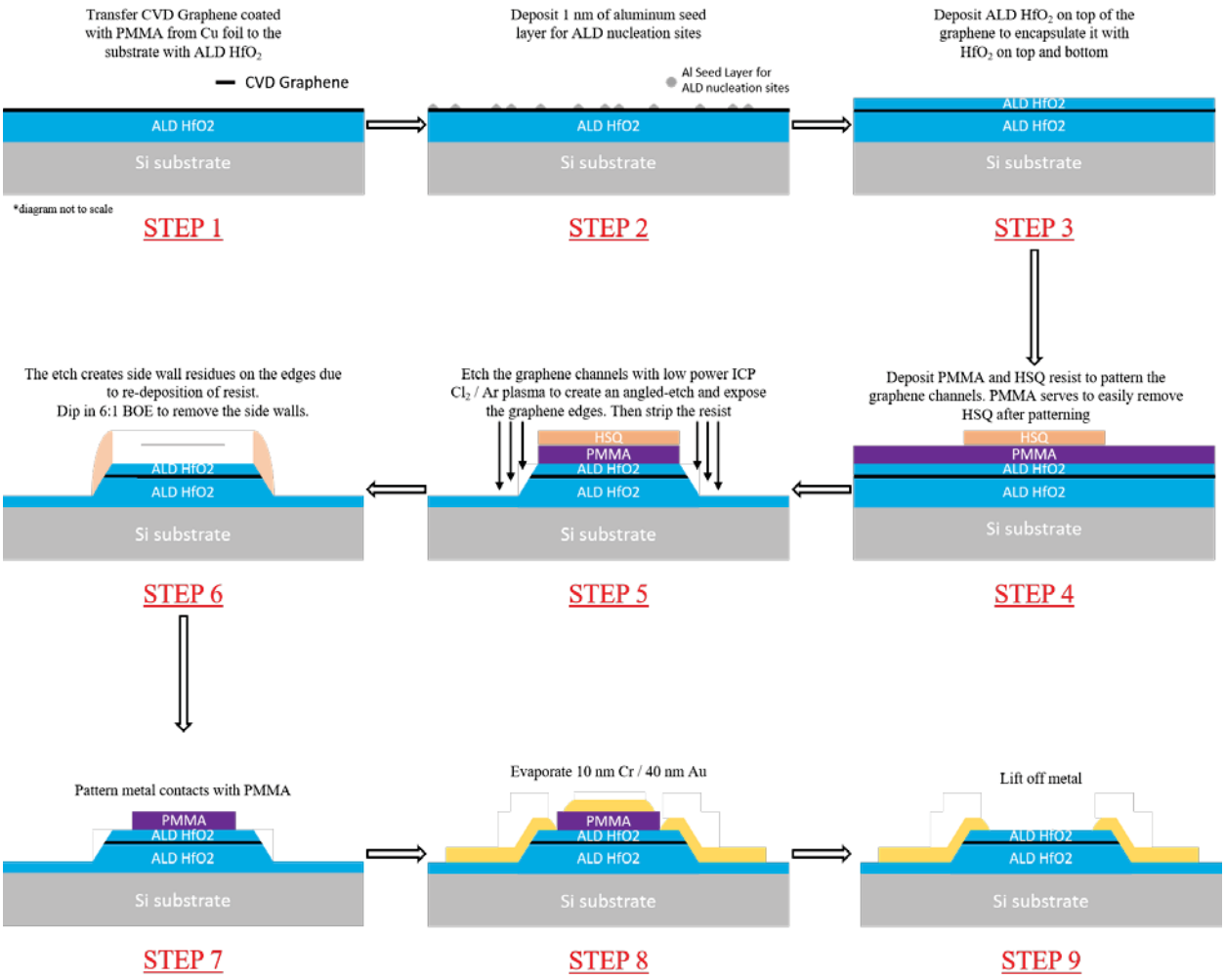

Figure 8: Fabrication Flow for Graphene Edge Contacts

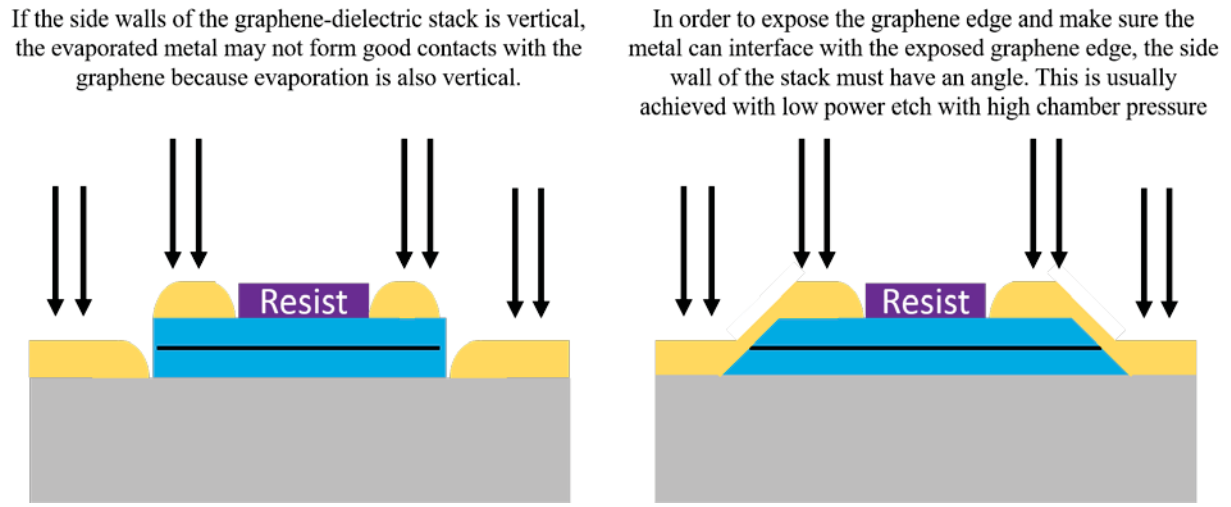

Figure 9: The Effect of Side Wall Angle in Forming Graphene Edge Contacts
The etch step (STEP 5 in Figure 8) is crucial in forming good edge contacts because the angled etch (right inset) exposes the graphene edge and allows metal to access that edge, as opposed to vertical side walls (left inset).

Another cricital step is to make sure that the exposed graphene edge is clean and residue free. The etching step consists of low power etch with Cl_2 and Ar based chemistry. The reason for using Cl_2 chemistry is that it has the relatively good selectivity for etching HfO_2, where volatile hafnium based etch byproducts are rare. Cl_2 does not chemically etch the mask resist, hydrogen silsesquioxane (HSQ), and therefore, redeposition of the resist due to physical etching accumulates on the side wall and contaminates the graphene edge. Because HSQ is easily removed in buffered oxide etch (BOE) while HfO_2 is etched slowly in BOE, a short BOE dip can remove this sidewall residues. Figure 10 shows the scanning electron microscope (SEM) image of the redespoited sidewalls, and how BOE dip can remove this residue.

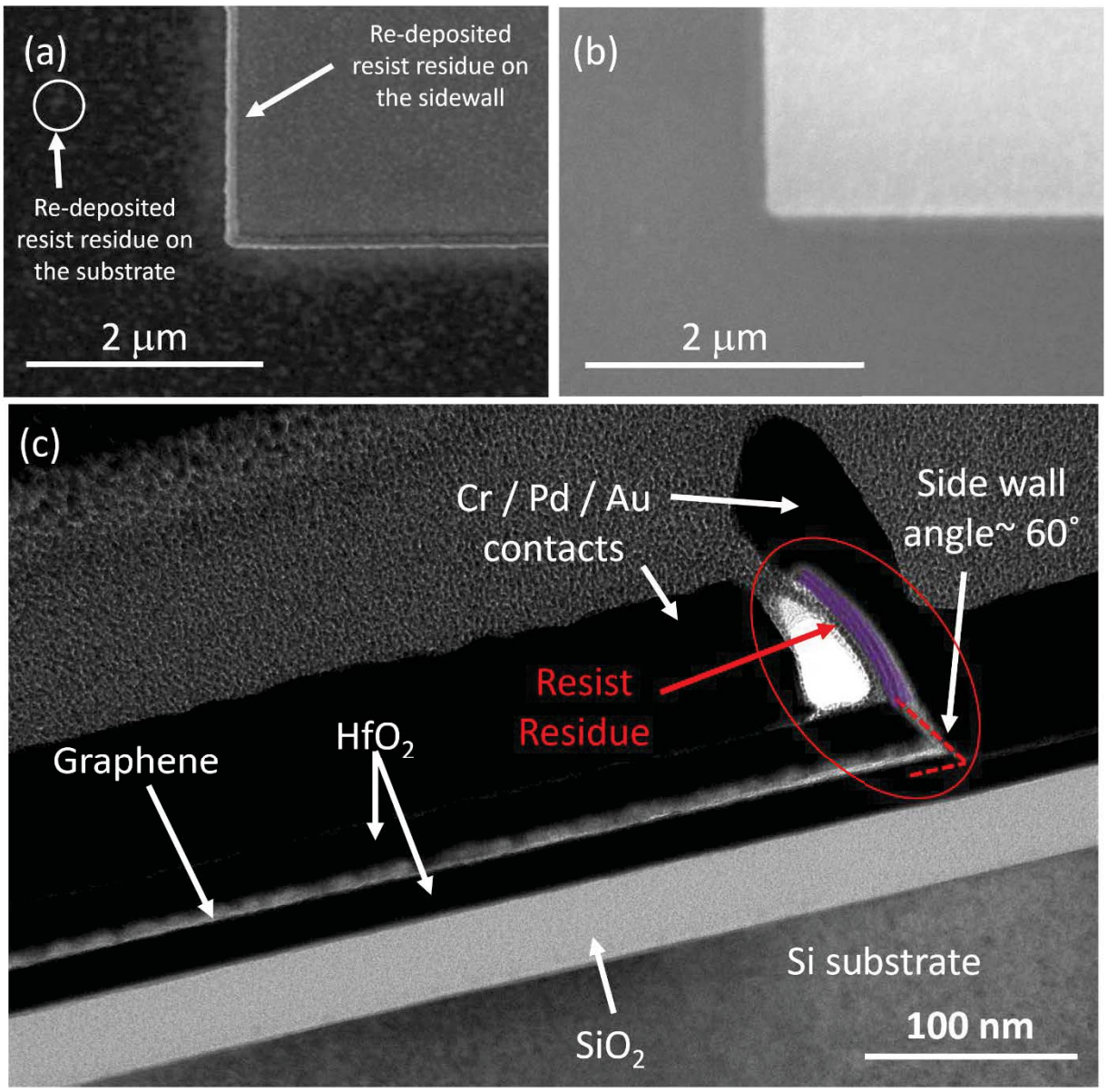

Figure 10: SEM Image of the Redespoited Sidewalls and how BOE Dip can Remove this Residue

(a, b) SEM images of the resist residue on the sidewall of the stack before and after the BOE dip, respectively. The hump on the stack in (a) as well as some speckles on the stubstrate is cleaned with BOE, as (b) clearly shows no humps and cleaner substrate. (c) Transmission electron microscope image of a cross-section of the fabricated graphene channel at the graphene-metal edge interface. This device was fabricated without removing the resist residue shown in (a). The purple (false-color) highlighted region is the resist residue on the side wall of the graphene stack, and it prohibits clean metal-graphene interface formation. The side angle of the stack is also clearly shown.

4. RESULTS AND DISCUSSION

4.1 Graphene Electro-Refractive Modulator

We report the experimental demonstration of the electro-refractive modulator based on graphene in the regime where absorption of graphene is modulated minimally (by less than 1 dB) while the phase is modulated strongly (by more than 0.05π in a small 100 μm device). We integrated the capacitor in a Si_3N_4-waveguide-based unbalanced MZI and extract the change in effective refractive index from the optical spectra at several voltages. For capacitor voltages less than 6.8 V, loss and phase modulation occur simultaneously, causing the MZI fringes to blue shift by approximately 1 nm, indicating an effective refractive index change of -1.4×10^{-3} for the entire graphene capacitor/waveguide structure (Figure 11). When higher voltages are applied ($6.8\ V \leq V \leq 7.5\ V$) and inter-band absorption stops due to the unavailability of vacant states, the MZI fringes red shift by approximately 0.3 nm indicating an effective index of 4×10^{-4}.

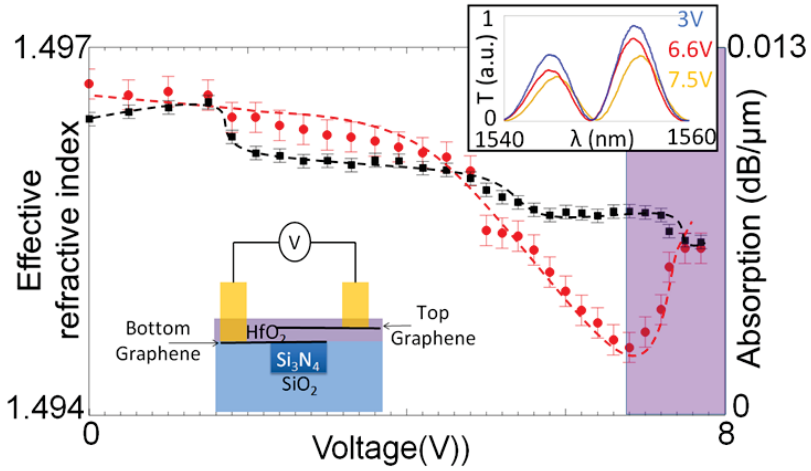

Figure 11: Electrical and Optical Measurements - Effective Index and Absorption Profile of the Propagating TE Mode with different Voltages Applied to the Graphene Capacitor on the Right Arm

Dashed lines serve as a guide to the eye. TOP INSET: Transmission response of the device shown in Figure 1(c) at different voltages applied across the top and bottom graphene electrode.

After subtracting the fiber-chip coupling losses, the insertion loss of the graphene modulator averages 0.07 dB/μm in the phase-only regime, for a total insertion loss of 7 dB. As shown inFigure 12, the variation of effective refractive index of the propagating mode in the presence of graphene follows the theoretically expected trend. RF measurements on the device at the different voltages indicate that the device behaves as a phase modulator between 6.8V and 7.5V with a 3-dB RC limited bandwidth of 640 MHz (Figure 13).

By fitting pur results to the theoretical predictions, we show that in one of the graphene layers, we achieve low absorption. When we increase the index change, the absorption decreases. In order to achieve low absorption and high index change, both the layers have to be doped intrinsically.

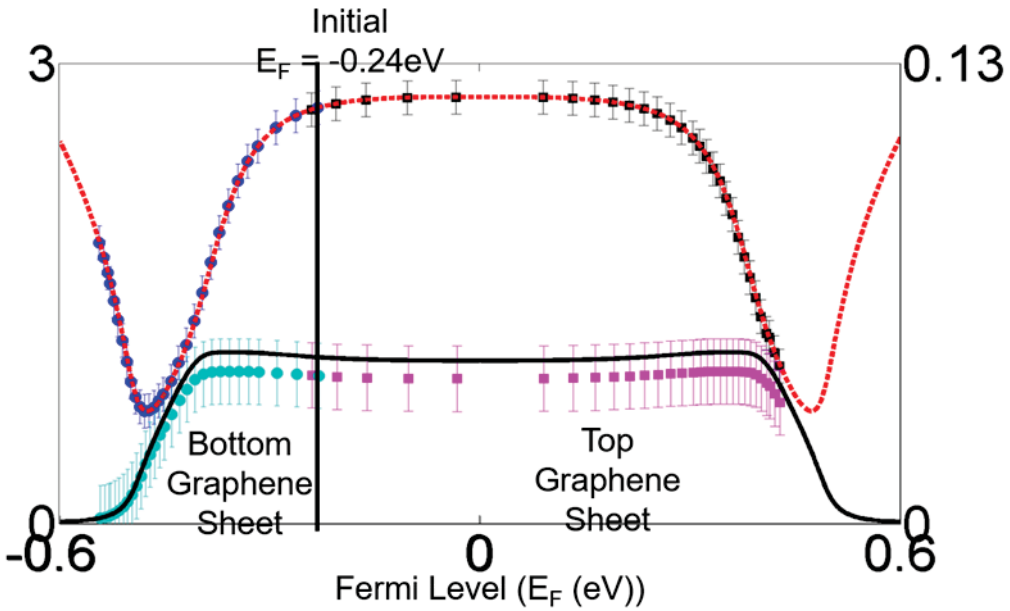

Figure 12: Electrical and Optical Measurements - Refractive Index and Absorption of Top and Bottom Graphene Sheets Obtained from Figure 2 and COMSOL Simulations
As seen, it is found that both the graphene sheets are doped to -0.24eV, due to which only the bottom sheet reaches the transparent regime, whereas the top sheet is still absorbing, thereby limiting the performance of the device.

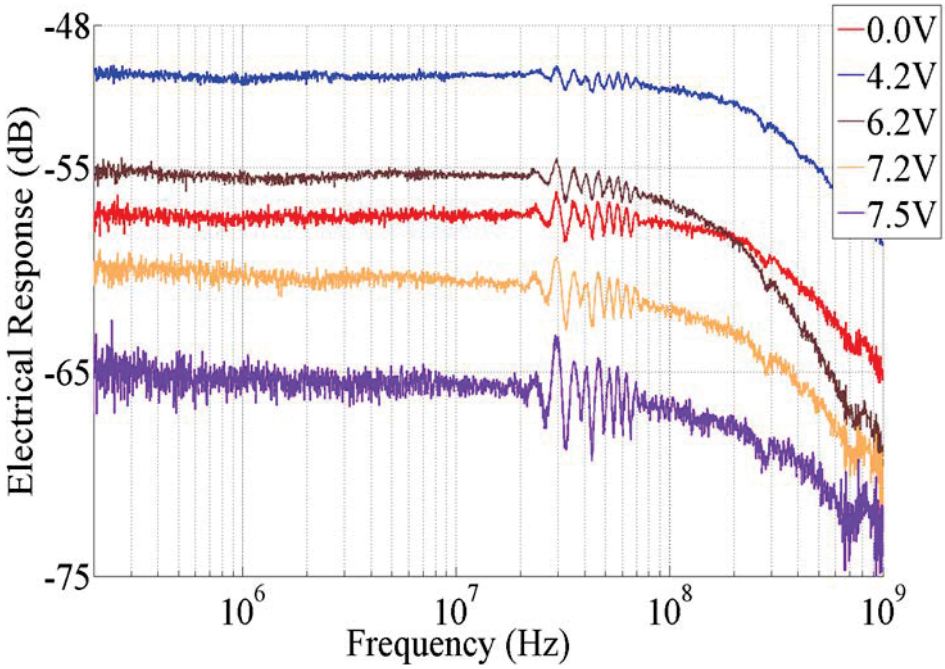

Figure 13: RC Frequency Response of the Capacitive Devices
The 3dB bandwidth for these devices is about 0.6 GHz.

4.1.1 Change in MZI Transmission after using Ammonium Persulfate

The experimental results obtained in the first fabrication run show that the top and bottom graphene sheets are p-doped to -0.24 eV, which causes only one of the graphene layers to be electrically tuned to the low loss regime, however the other graphene layer is still absorbing. It was seen that the transfer process contributes to the doping concentration of graphene. Initially, the back Cu was etched using $FeCl_3$ solution. The electrolytic reaction lead to replace the Cu^{2+} ions with Fe^{3+}, which doped the graphene, which lead to the graphene layer being doped. We decided to use ammonium persulphate to etch the backside Cu, which reduces the doping on graphene. We fabricate devices as shown Figure 14, using the new graphene wet transfer method.

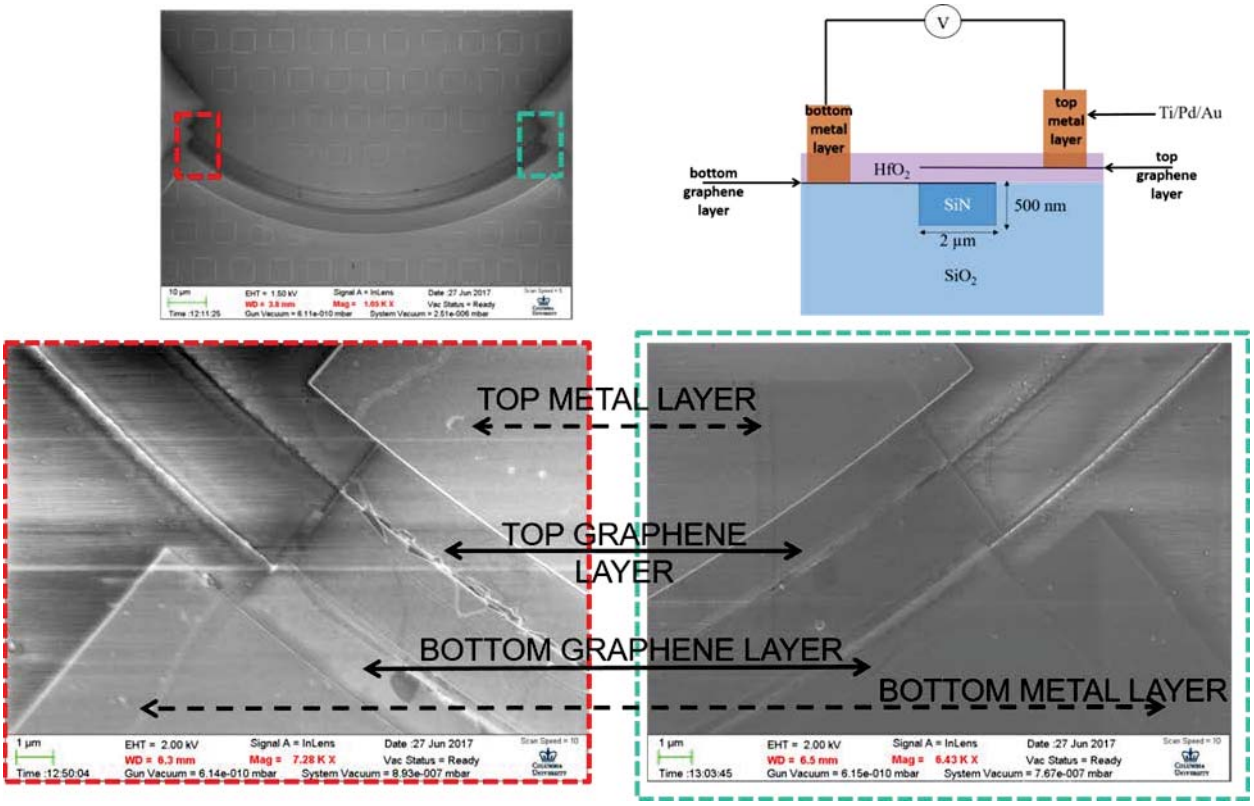

Figure 14: Graphene Devices Fabricated using New Ammonium Persulphate Transfer Method

The current devices have dimensions of 2 µm × 532 nm as seen in Figure 14. The MZI transmission is measured by applying voltage across 200um of graphene-HfO_2-graphene capacitor on one arm of balanced MZI (Figure 14). Figure 15 shows the trend for graphene absorption with voltage across the devices. The extracted graphene absorption as a function of the voltage applied across the top and bottom sheet is shown in Figure 16.

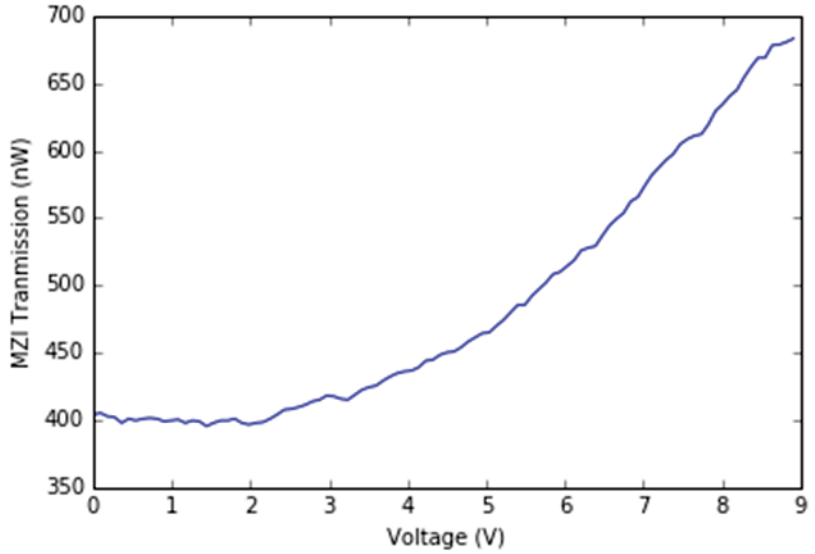

Figure 15: MZI Transmission with Voltage

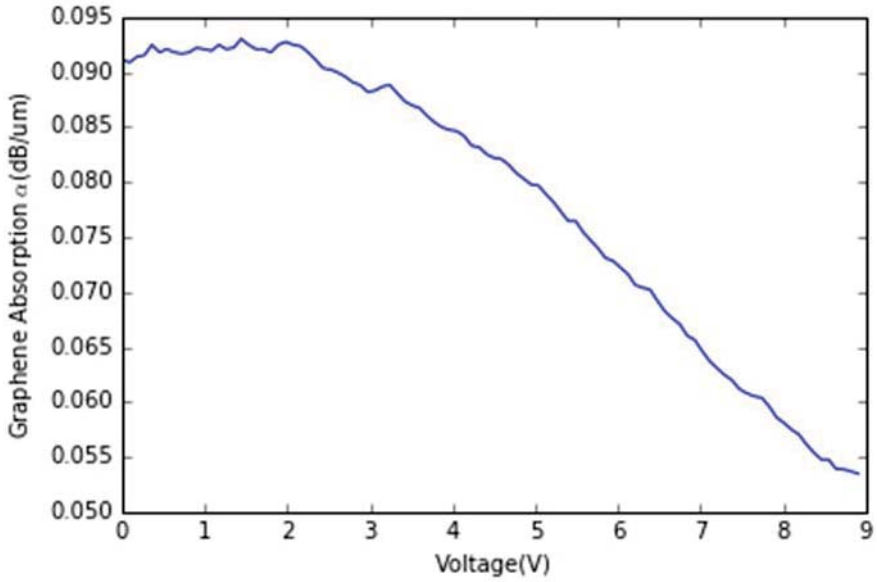

Figure 16: Extracted Graphene Absorption Modulation at different Bias Voltages at 1550 nm

We demonstrate the reduction in initial doping of the graphene layer by measuring the transmission at the output of an on-chip MZI when a bias voltage is applied to 200 um graphene length on one arm of a balanced interferometer at 1560 nm. The hysteresis in the graphene devices have also been measured by sweep the voltage across 32 nm of HfO_2 from 0 to 9 V, 9 V to 0 V, 0 V to -9 V, -9 V to 0 V.

When graphene is initially p-doped, due to presence of inherent charges on the monolayer graphene, the output transmission power is different when the polarity of voltage applied across the graphene capacitor is reversed. Due to the presence of inherent charges in graphene, the

graphene monolayer becomes more transparent under one voltage polarity as compared to the reverse polarity.

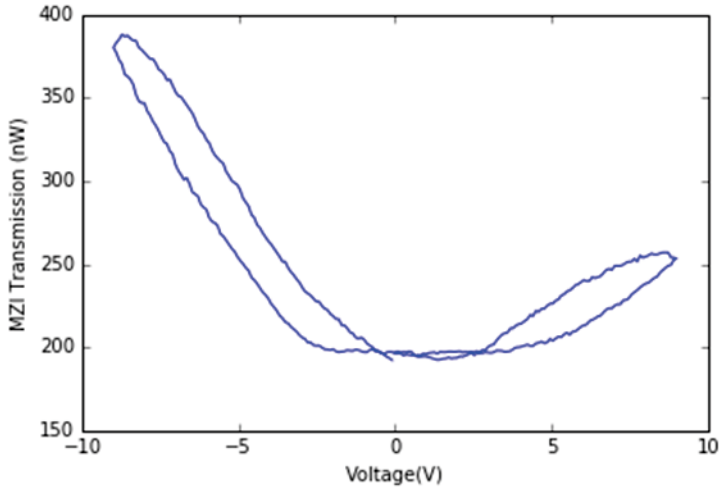

Figure 17: MZI Transmission for Devices when Graphene is initially p-doped

As expected from recent fabrication run – when the graphene is undoped, the MZI transmission output remains the same when the voltage polarities are reversed.

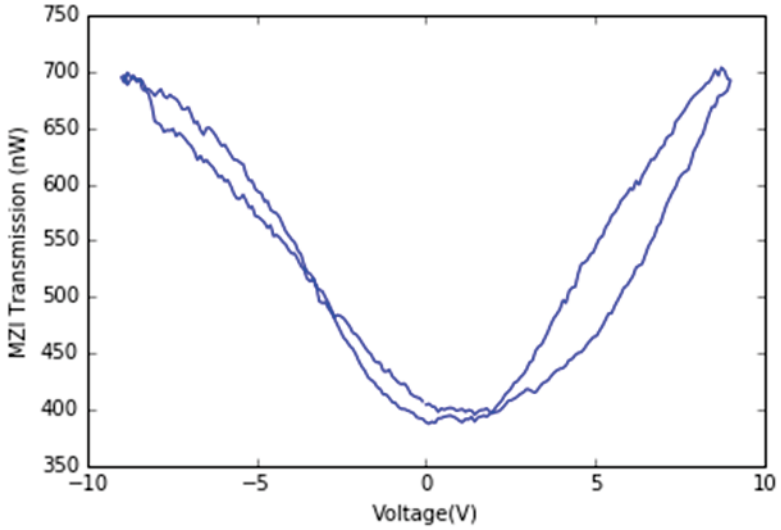

Figure 18: MZI Transmission when Graphene is Unbiased initially

Through COMSOL simulations on a 2 um wide x 530 nm tall waveguides, the effective index change iis much smaller than for waveguides of 1 um wide x 330 nm, but the absorption scales as before (Figure 19). The devices designed in this run have zero arm length difference between the two arms.

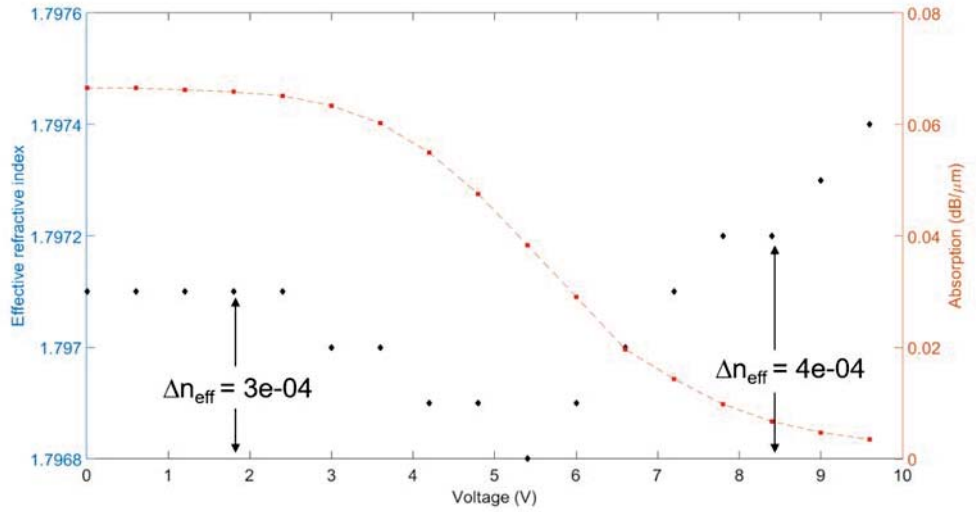

Figure 19: COMSOL Simulated Effective Index Change for Waveguide Configuration 2 um Wide x 530 nm Tall Waveguides

In a balanced Mach-Zender interferometer with balanced arms, the MZI transmission response is given by

$T = \left|1 + e^{-\Delta\alpha_g L_g - j\Delta\beta_g L_g}\right|^2$, where $\Delta\alpha_g = \alpha_g(V) - \alpha_g(0)$, $\Delta\beta_g = \beta_g(V) - \beta_g(0)$ and $L_g = 200\ \mu m$.

Using the change in effective index and absorption in graphene integrated waveguide (COMSOL simulation), Figure 20 describes the trend in the Transmission response with different voltage V. Unfortunatelly, in this wavelength range the absorption has more effect than the effective index and overshadows the phase change effect in a balanced Mach-Zender.

Experiments were done by applying a bias voltage on graphene-HfO_2-graphene capacitor on one arm of a balanced Mach-Zender and the MZI transmission response is recorded in Figure 21. Substrate was heated to 30 C. As seen, the effect of change in absorption can be illustrated as following. The multiple peaks are due to fabry perot reflections at the mode splitters (multimode interference (MMI)). The extracted absorption fit against the theoretically obtained value in Figure 22.

- The trend of change in absorption of graphene with applied voltage is extracted from the experimental results at a wavelength of 1570 nm.
- The extracted $\epsilon_R = 12$ for HfO_2 with an initial doping of -0.2eV. Dielectric thickness = 30nm.

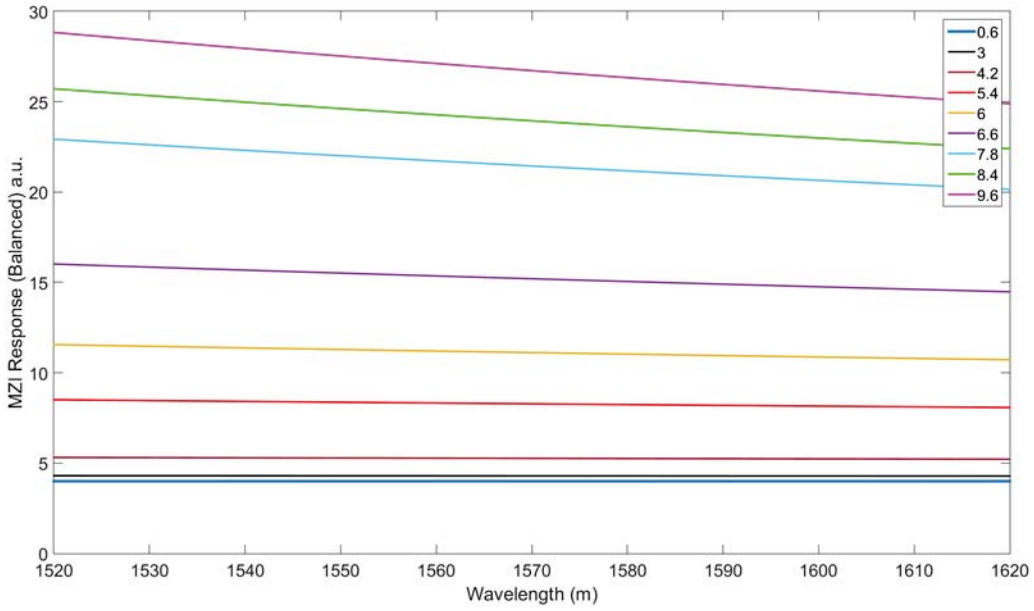

Figure 20: Theoretical Transmission in a balanced Mach Zehnder at different Voltages Applied across the Top and Bottom Electrode

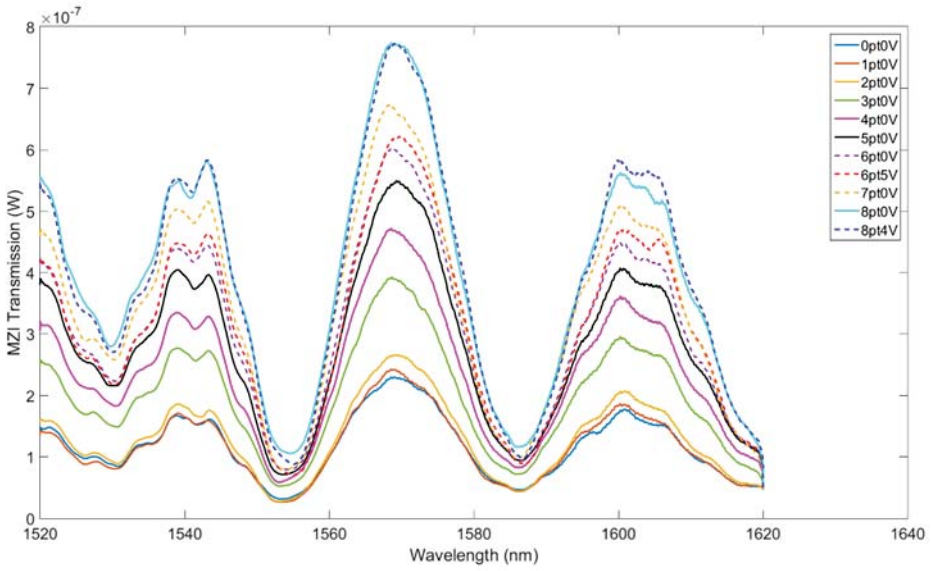

Figure 21: Measured Transmission vs Wavelength at different Bias Voltages when the Substrate is Heated to 30 C

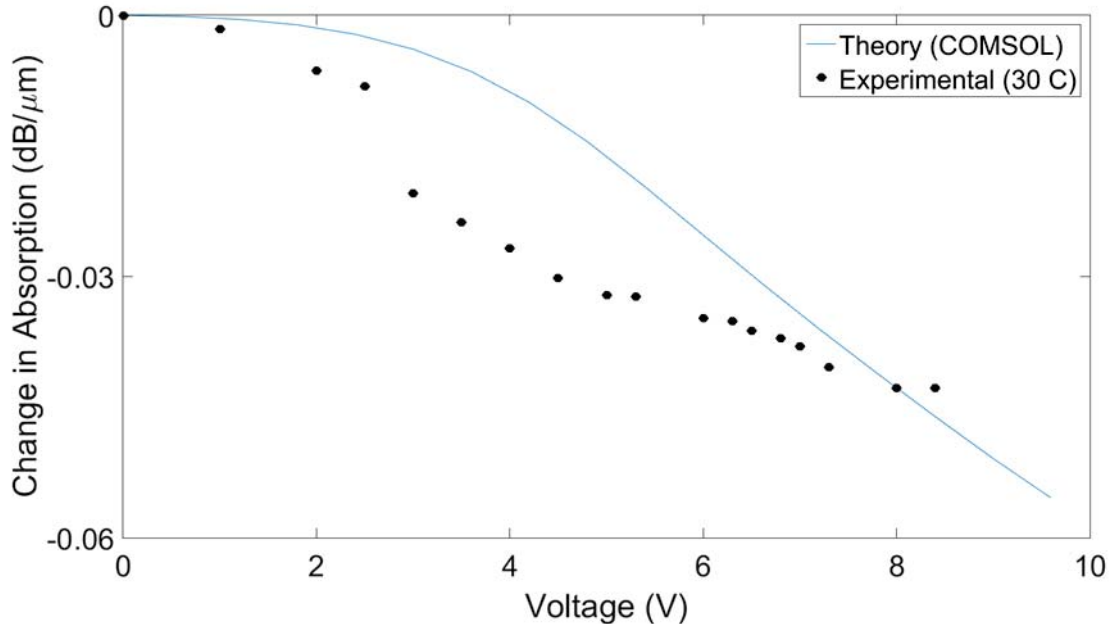

Figure 22: Extracted Aborption in Graphene vs Voltage and Comparison with Theory

4.1.2 Mid-Infrared Modulation by Graphene

In the mid-infrared (IR) we expect a stronger graphene response since in order to reach the transoparenmcy region one needs much smaller voltage. The MZI response for the graphene devices were tested at different mid-IR wavelengths (1.7 – 2.642 um) and shown in Figure 23. As expected we observe that with increased applied voltage, the extinction ratio increases as the graphene becomes more transparent with high bias lengths.

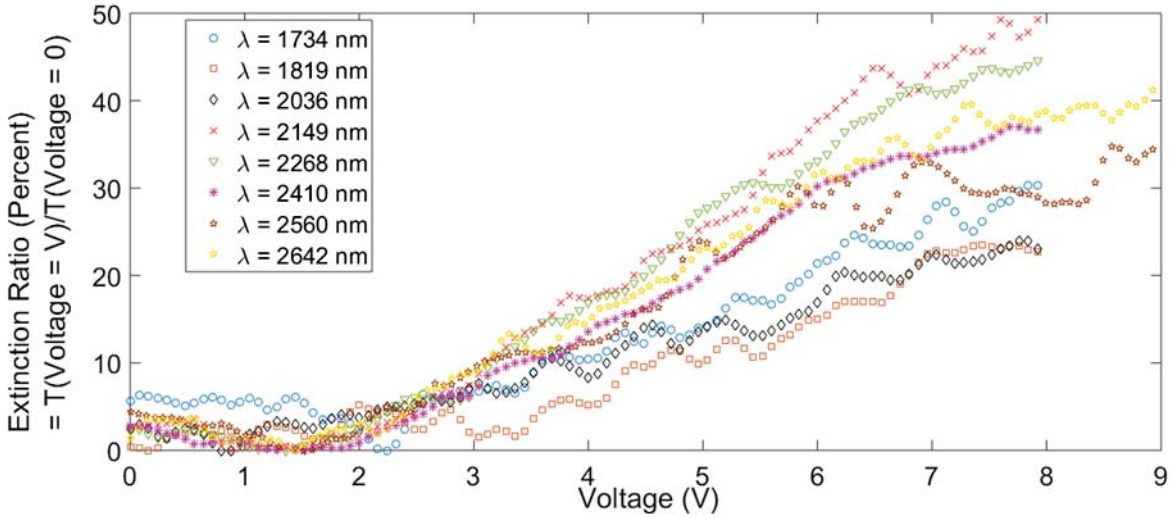

Figure 23: MZI Transmission Output Extinction Ratio vs Voltage for Mid-IR Wavelengths *(1.7 – 2.6 um)*

4.2 Graphene Edge Contacts

In order to show the importance of optimizing the process flow, Figure 24 shows the contact resistance measured from the first set of devices, where the resist residues on the stack sidewalls, as described by Figure 10a and c, are not removed by BOE. As shown by the measurements this set of devices had high contact resistance of 28 kΩ-μm due to the sidewalls preventing high quality metal-graphene interface.

Figure 25 shows the resistance measurements taken from a second set of devices for which the process was optimized, and where the sidewall residues were removed with BOE to clean the exposed graphene edge. The resistance values are normalized with respect to the width at various graphene channel lengths for simpler contact resisntane extraction. The extracted contact resistance is 1.2 kΩ-μm without any external carrier doping to the graphene, which is an order of magnitude improvement from the previous set of devices with sidewall residues. Note that contact resistance is dependant on carrier doping of the graphene [11], which means at higher carrier doping (thus higher fermi levels), the contact resistance might further derease. For example, Gahoi et al [11] showed that the contact resistance at Dirac point, 2.1 kΩ-μm, was further reduced to 92 Ω-μm when the channel was heaviliy p-doped by applying a back gate voltage, which is approximately one order of magnitude improvement.

Assuming we can achieve similar magnitude of improvement in our current contact resistance as in Ref. [11], which is about 20X improvement, our contact resistance could be about 60 Ω-μm which is very close the best state of the art CVD graphene contact resistance [12]. When applied to the devices that we previously demonstrated based on ring resonators [7], we expect to achieve a bandwidth of at least 50GHz. Note that the distribution of the resistance values at 10 μm and 30 μm is large and this may add some uncertainty to the contact resistance measurement. This is primarily due to low quality graphene transfer, resulting in tears, wrinkles, and residues. Figure 26 is a optical microscope image describing these problems with the graphene transfer. The tears can both increase the resistance both the channel and the edge contacts by reducing the effective width of the contact. Polymer residues resulting from the transfer are defects and scattering points for carriers in the channel, increasing the total resistance of the device, as indicated by very high sheet resistance from the TLM measurement in Figure 25.

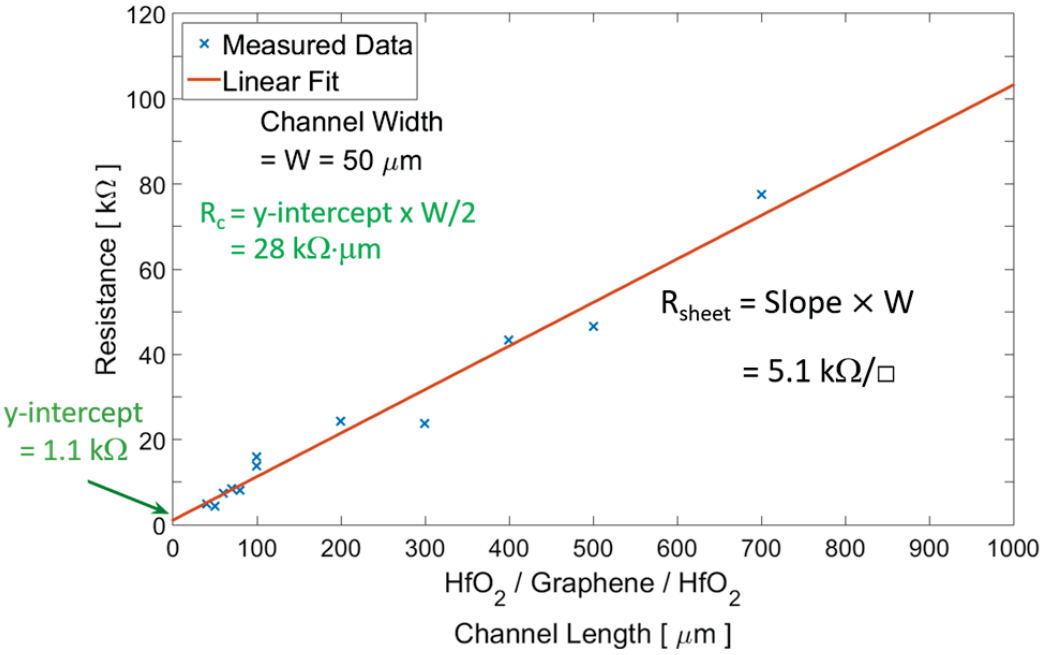

Figure 24: First Generation of Graphene Edge Contacts

*Resistance is plotted with respect to graphene channel length. The blue dots are measured values and orange line is the linear fit to the data. The extracted contact resistance from the linear fit of the data is 28 k**Ω-μ**m.*

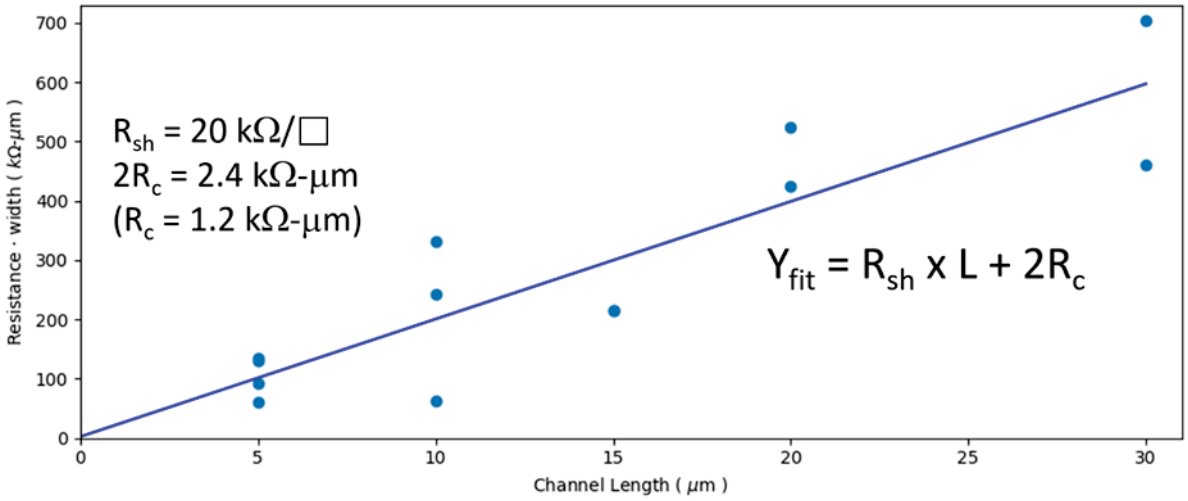

Figure 25: Resistance Normalized to Width with Respect to graphene Channel Length

*The extracted contact resistance from the linear fit of the data is 1.2 k**Ω-μ**m.*

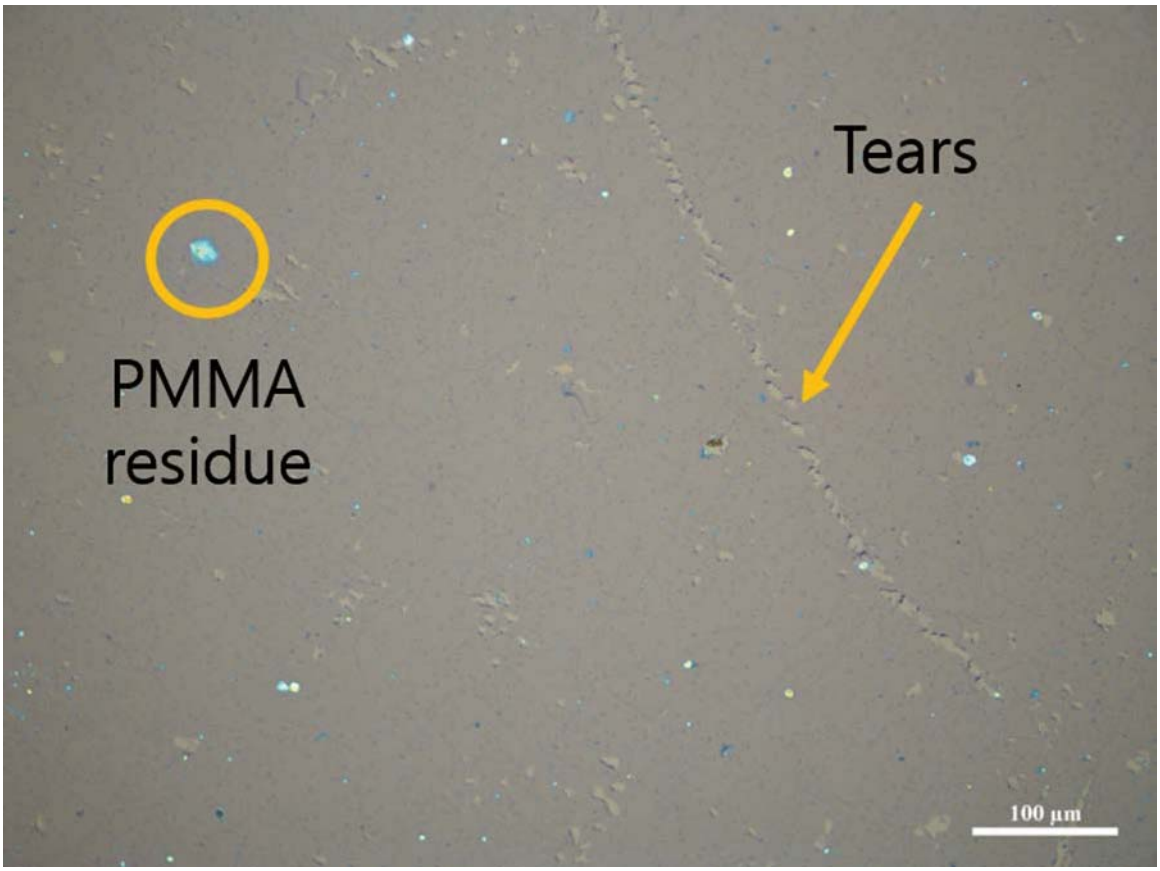

Figure 26: CVD Graphene Transfer Tears and Residues
The density of tears in the graphene sheet increases the resistance of graphene devices and inconsistent values of resistances. Poly(methyl methacrylate) (PMMA) residues also increase the resistance of the devices.

5. CONCLUSIONS

Here we show that graphene can provide electro-optic properties to traditionally passive optical materials. We show a 0.6 GHz electro-refractive modulator with $V_{\pi}L$ of 1.4 Vcm based on graphene layers integrated with a silicon nitride waveguide. Under applied voltage, we experimentally reach the theoretically predicted anomalous regime of the graphene index, where the real part of the index is changed by 250 percent while its imaginary part (i.e. the absorption) remains largely unchanged. In addition, we show a process for achieving low contact resistance using CVD graphene for scalable graphene based electro-optical devices with 1.2 kΩ-μm Dirac point contact resistance, enabling high speed devices,

Our work developed the critical steps for a platform consisting of 2D materials embedded in waveguides, in which electrostatic doping is used for tuning the dielectric properties of the guiding structures. Graphene as well as other 2D materials and thin films, have been shown recently to exhibit high tunability of index with doping. This platform could enable ultrafast devices with unprecedented low power. These critical steps are summarized below:

(I) a process flow for fabricating edge contacts with sufficient low contact resistance to enable modualtors beyond 50GHz.
(II) Waveguide with embedded ghraphene with a geometry that enbales ultra- high electrostatic doping, enabling.
(III) Developed doping-free transfer of graphene, for which doping is only induced electrostatiocllay, and therefore ultra low absorption can be acheievd. We show absorption below 2dB/mm, or less than 5% absorption for a length of 100 microns-more than sufficient to achieve full modulation.

6. RECOMMENDATIONS

Future work:

- In order to demonstrate a phase modulator based on these preliminary results, an optimized geometry, for which the Mach Zehnder operates as a single mode (instead of the multi-mode structures we measured) should be designed and tested.
- Using our developed graphene edge contacts that enable high bandwidth, one could fabricate compact resonator-based modulators and demonstrate ultra-high bandwidth devices with speeds well beyond the typical ~30-40GHz silicon modulators. In addition these edge contacts could be applied to longer strcutures such as Mach Zehnders, as long as the graphene transfer process is further optimized to ensure low sheet resistance.
- Based on the graphene high level of transparency that we achieved, one could use Graphene as effective contact for photonic devices. This can be especially suefull when embedding 2D materials that require a speicifc doping type (p or n) in order to tune their optical properties.
- Measure edge contact resistance under electrostatic doping. Higher doping is expected to reduce the resistance.

7. REFERENCES

1. Y.-C. Chang, C.-H. Liu, C.-H. Liu, Z. Zhong, and T. B. Norris, Appl. Phys. Lett. **104**, 261909 (2014).
2. T. Stauber, N. M. R. Peres, and A. K. Geim, Phys. Rev. B **78**, 085432 (2008).
3. M. Lafkioti, B. Krauss, T. Lohmann, U. Zschieschang, H. Klauk, K. v. Klitzing, and J. H. Smet, Nano Lett. **10**, 1149 (2010).
4. J. W. Suk, W. H. Lee, J. Lee, H. Chou, R. D. Piner, Y. Hao, D. Akinwande, and R. S. Ruoff, Nano Lett. **13**, 1462 (2013).
5. Y.-W. Tan, Y. Zhang, K. Bolotin, Y. Zhao, S. Adam, E. H. Hwang, S. Das Sarma, H. L. Stormer, and P. Kim, Phys. Rev. Lett. **99**, 246803 (2007).
6. V. Sorianello, G. D. Angelis, T. Cassese, M. Midrio, M. Romagnoli, M. Mohsin, M. Otto, D. Neumaier, I. Asselberghs, J. V. Campenhout, and C. Huyghebaert, Opt. Express **24**, 29984 (2016).
7. C. T. Phare, Y.-H. Daniel Lee, J. Cardenas, and M. Lipson, Nat. Photonics **9**, 511 (2015).
8. M. Liu, X. Yin, E. Ulin-Avila, B. Geng, T. Zentgraf, L. Ju, F. Wang, and X. Zhang, Nature **474**, 64 (2011).
9. C. Hwang, D. A. Siegel, S.-K. Mo, W. Regan, A. Ismach, Y. Zhang, A. Zettl, and A. Lanzara, Sci. Rep. **2**, 590 (2012).
10. L. Wang, I. Meric, P. Y. Huang, Q. Gao, Y. Gao, H. Tran, T. Taniguchi, K. Watanabe, L. M. Campos, D. A. Muller, J. Guo, P. Kim, J. Hone, K. L. Shepard, C. R. Dean, Science **342**, 6158 (2013).
11. A. Gahoi, S. Wagner, A. Bablich, S. Kataria, V. Passi, M. C. Lemme, Solid-State Electron. **125**, 234-239 (2016).

LIST OF ABBREVIATIONS, ACRONYMS, AND SYMBOLS

ACRONYM	DESCRIPTION
2D	two-dimensional
ALD	atomic layer deposition
BOE	buffered oxide etch
CVD	chemical vapor deposition
DC	direct current
EO	electro-optic/optical
HSQ	hydrogen silsesquioxane
IR	infrared
MMI	multimode interference
MZI	Mach-Zender interferometer
PMMA	poly(methyl methacrylate)
RC	resistor-capacitor
RI	refractive index
SEM	scanning electron microscope
TE	transverse electric
TLM	transmission line method